Chemical Engineering Journal 518 (2025) 164686

Contents lists available at ScienceDirect

Chemical Engineering Journal

journal homepage: www.elsevier.com/locate/cej

Simulating the influence of Cu impurities on the performance of NMC811 cathodes for *re*-synthesis from recycling☆

Antonino Giarrizzo [a], Arcangelo Celeste [a,b,*], Marco Agostini [c], Pier Giorgio Schiavi [a], Graziano Di Donato [d,e], Thomas Diemant [d,e], Pietro Altimari [a], Micol Di Veroli [a], Francesca Pagnanelli [a,b,f], Sergio Brutti [a,b,f,g]

[a] Department of Chemistry, Sapienza University of Rome, P.le Aldo Moro 5, 00185 Rome, Italy
[b] ALISTORE European Research Institute (ALISTORE ERI) - Department of Chemistry, Sapienza University of Rome, P.le Aldo Moro 5, 00185 Rome, Italy
[c] Department of Chemistry and Drug Technologies, Sapienza University of Rome, P.le Aldo Moro 5, Rome 00185, Italy
[d] Helmholtz Institute Ulm (HIU), Helmholtzstrasse 11, 89081 Ulm, Germany
[e] Karlsruhe Institute of Technology (KIT), P.O. Box 3640, 76021 Karlsruhe, Germany
[f] Centro di Riferimento Nazionale per i Sistemi di Accumulo Elettrochimico di Energia (GISEL), INSTM, Florence, Italy
[g] Istituto dei Sistemi Complessi (ICS-CNR), CNR, Rome, Italy

ARTICLE INFO

Keywords:
Li-ion batteries
Recycling process
Cu impurities
NMC
Oxalate co-precipitation

ABSTRACT

The recycling of Lithium-Ion Batteries (LIBs) has gained increasing significance but presents considerable challenges. During the mechanical crushing and sorting of spent LIBs, the resulting black mass exhibits a complex chemical composition. Despite costly purification processes, impurities can easily contaminate the final recycled materials. Understanding the role of these impurities is crucial, as they can impact the electrochemical performance, material stability, and durability of the recovered active materials.

This study aims to investigate the impact of copper impurities from spent LIBs on the physical-chemical and electrochemical properties of NMC811 ($LiNi_{0.8}Mn_{0.1}Co_{0.1}O_2$) and evaluate how crystallization procedures influence these properties. NMC811 was synthesized via oxalate co-precipitation, enabling precipitation without additional complexing agents or an inert atmosphere, aspects that make the synthesis promising for integration into closed-loop recycling of LIBs. Specifically, two levels of Cu^{2+} doping (0.66 at.% and 1.09 at.%, relative to the total metal concentration in the precursor blend) were investigated and compared with NMC synthetized in absence of Cu. These doping levels were chosen based on the copper concentrations in leachates obtained from dust in a pilot plant. Physical-chemical analysis revealed that copper can be incorporated into the NMC structure without phase segregation, and low copper concentrations can enhance the electrochemical performance, improving both specific capacity and capacity retention.

1. Introduction

Lithium-Ion Batteries (LIBs) are a well-established and widespread technology [1] thanks to their high energy density, good cycle life and a low level of self-discharge. Today, the potential applications of LIBs have been extended to electric vehicles (EVs) and hybrid electric vehicles (HEVs), therefore, they play a crucial role in the energy transition and their production/utilization is expected to increase further in the future [2]. Hence, the production, diffusion and obsolescence of an increasing quantity of Li-ion cells will lead to significant quantities of exhausted LIBs, in consideration of the varying lifetimes for batteries in different applications (smartphones: about 2 years, other consumer electronics 3–4 years and electric vehicles >10 years) [3]. Furthermore, spent LIBs contain many toxic but also valuable materials, including heavy metals such as copper, cobalt, nickel, and hazardous organic chemicals such as electrolytes and separators [4,5]. Their disposal in landfills can allow heavy metals, fluorine, phosphorous and sulphur to seep into groundwater, resulting in a long-term environmental impact [6]. In contrast, a full recycling of electrodes collected post-mortem from spent batteries would allow the processing of a considerable amounts of metallic and

☆ This article is part of a Special issue entitled: 'Electrochemical Energy' published in Chemical Engineering Journal.

* Corresponding author at: Department of Chemistry, Sapienza University of Rome, P.le Aldo Moro 5, 00185 Rome, Italy.
E-mail address: arcangelo.celeste@uniroma1.it (A. Celeste).

https://doi.org/10.1016/j.cej.2025.164686
Received 7 March 2025; Received in revised form 5 June 2025; Accepted 8 June 2025
Available online 9 June 2025

non-metallic species thus feeding important secondary sources for addressing the shortage of natural resources [7]. Consequently, the design and implementation of the sustainable recycling processes for LIBs has become one important issue in battery industry [8]. As highlighted by the United Nations Sustainable Development Goals (SDGs), efficient LIB recycling directly supports SDG 12: Responsible Consumption and Production, SDG 13: Climate Action, SDG 9: Industry, Innovation, and Infrastructure, and SDG 7: Affordable and Clean Energy by reducing resource dependency, minimizing environmental impacts, fostering technological innovation, and facilitating the transition to a more sustainable and resilient energy infrastructure [9,10]. Moreover, it is also important to underline that the recycling of valuable materials from end-of-life lithium-ion batteries has been identified by the European Union as one possible strategy to preserve environment and make a better use of resources thus reducing human footprint [11]. This is particularly important given the emerging needs of the battery market and the entry of new European players, who aim to use recycled materials to meet production demands.

Nowadays, there are three demonstrated recycling methodologies [12,13]: pyrometallurgy, hydrometallurgy, and direct recycling [8,14–17]. Among them, the hydrometallurgical process exhibits many advantages, including the high yield of recovered cathode materials, low electrical energy costs, and exhaust emissions [18]. Hydrometallurgy proceeds through three major steps: physical pretreatment for the recovery of black mass (i.e. the powder made up of cathodic and anodic components), metal extraction in solution by leaching, and metal recovery by precipitation [19–21]. Innovative hydrometallurgical recycling processes integrate end of life treatment with resynthesis of new cathode materials [22,23]. The main idea of these processes is to directly synthesize a cathode precursor from the solution of the extracted metals (Co, Ni, Mn). This way, the complex separation of the different metals can be excluded, reducing the costs and the environmental impact. However, the production of positive electrode materials from black mass results in the incorporation of small quantities of spurious metals, such as copper, aluminum, and iron, in the metal blend (i.e. Li, Co, Ni, Mn), which originate from the battery cases, current collectors, surface coatings, and separators. This contamination originates from the inefficacy of the separation process of the black mass [24–28]. The incorporation of undesired amounts of spurious metals to the final active material stoichiometry alters their physical and chemical properties and may impact the resulting battery performance. Apparently recycled layered oxides can tolerate different impurity levels for different dopants (e.g., 0.2–3 % for Al, 0.5 % for Fe, and 2.5–6 % for Cu) having limited impact on performance [5,26,29–31]. Overall, Cu impurities originating from the anode current collectors, represent a challenging case. In fact, starting from the hydrometallurgical digest solution, Al^{3+} and Fe^{3+} ions can be selectively precipitated by controlling the solution's pH, whereas Cu^{2+} hydroxides suffer from larger solubility constants. Accordingly, the effective removal of Cu^{2+} requires increasing the pH to values at which also Ni^{2+}, Mn^{2+}, and Co^{2+} can precipitate, thus reducing the recovery efficiency of these valuable metals [25]. To provide context, the total copper contamination in recycled materials depends on the specific recycling process. We have included typical contamination levels from various recycling techniques in Table S1 to offer insight into this variation. On the other hand, previous studies have evidenced that the copper impurities can be tolerated and even yield an improvement in the electrochemical performance of the synthesized cathode materials in terms of stabilization of the layered structure, and the promotion of a facile lithium-ion transport in the solid state. Impurity levels approaching 5 at.% Cu can be incorporated as dopants into the NMC layered lattice and lead to an increase in the Li-transition metals cation mixing degree [4,32]. Smaller Cu- doping (e.g. 0.2 at.% and 1 at. %) limits the Li/Ni mixing in the lattice thus improving the cycling stability and rate capability of NMC [33,34].

The correct amount of copper (Cu) is crucial for enhancing the cathode properties. Excessive Cu impurities, however, can negatively impact its structure and performance [4,34]. For instance, high Cu concentrations can lead to a lower tap density in the electrode due to the formation of smaller, thinner primary particles and more porous secondary particles. Additionally, Cu impurities may increase cation mixing, which in turn could result in poor rate capability and cycle performance. In terms of safety, Cu impurities can be introduced in the form of metallic Cu, which has been associated with sudden cell failure shortly after charging [35]. This occurs due to Cu dissolution into the organic electrolyte, migration across the separator from the cathode, and subsequent deposition onto the surface of the lithium metal anode. As a consequence, the understanding of the impact of copper on the recycled materials crystal structure and electrochemical performance in Li-ion cells is crucial to optimize the operating conditions of hydrometallurgical resynthesis processes. This work investigates the effect of Cu impurity on the performance of NMC811 cathode materials synthesized by simulating a recycling process. Specifically, we deliberately incorporate well known amounts of Cu^{2+} impurities into NMC811 material by modifying an oxalate co-precipitation process (OCP) previously demonstrated by some of us in a full recycling process from a black mass [23]. In particular, two levels of Cu^{2+} doping, 0.66 at.% and 1.09 at.% in respect to the total metal concentrations in the precursors blend, have been adopted. These doping values have been chosen considering the expected copper concentrations found in the solution obtained by acid-reductive leaching of the black mass from for a physical pretreatment plant[1] [36]. In this study, 1.09 % of Cu was found in the leachate of the black mass without further purification, while 0.66 % was the concentration observed after a purification step at a pH of 5. In addition, the effect of pH during the co-precipitation process was investigated. Importantly, this work demonstrates the successful use of oxalic acid as a precipitating agent, which not only enables the synthesis of high-quality materials but also offers a cost-effective and environmentally friendly alternative to conventional inorganic bases such as sodium hydroxide or lithium hydroxide. This method eliminates the need for additional complexing agents or inert atmospheres, simplifying the overall synthesis process [37,38]. Moreover, we found that the copper impurities retain, which could be a detrimental impurity, can actually enhance the electrochemical performance of the final product.

2. Experimental section

2.1. Materials synthesis

All NMC samples were synthesized via oxalate co-precipitation method. Weighted amounts of $NiSO_4 \cdot 6H_2O$ (98 %, Thermo Scientific, Waltham, MA, USA), $CoSO_4 \cdot 7H_2O$ (98 % VWR Chemicals, Radnor, PA, USA) and $MnSO_4 \cdot H_2O$ (99 %, Thermo Scientific, Saint Louis, MO, USA) were fully dissolved in deionized water (DI water), with the desired molar ratio of 8:1:1, formulating a 2 M metal sulfate solution at room temperature. An aqueous solution of oxalic acid (1.5 M, Thermo Scientific, MA, USA), was added for chelation and to enable the precipitation of the metals oxalates (i.e. simulated synthesis precursors). Oxalic acid is used because is not expensive, eco-friendly and able to form control the nucleation and grain growth [39,40].

Precursor synthesis was performed in a jacketed reactor (Lenz Laborglas GmbH & Co. KG, Wertheim, Germany) (height: 8 cm, diameter: 6.2 cm, volume: 100 mL) at 60 °C using mechanical stirring (1000 rpm) for 24 h. This time has been chosen because, from the literature, lead to the formation of ordered structure, reduces cation mixing, and improves the crystallinity [41,42].

The precipitate is separated by centrifugation and then dried for 24 h at 60 °C to obtain a fine powder further calcined in air at 500 °C (heating rate 2 °C/min) for 5 h. The resulting black powder was mixed, in a mortar, with $LiOH \cdot H_2O$ as a source of lithium. Since lithium source also impacts the final product, lithium hydroxide was chosen because it typically exhibits the best electrochemcial performance and for its lower melting point [43,44]. An excess stoichiometric ratio of 10 % $LiOH \cdot H_2O$

was used to compensate the inevitable possible loss of lithium during calcination at high temperature via gas phase or via dissolution in the alumina crucible. The composite material was calcined in air at 500 °C (2 °C/min) for 6 h and 850 °C (3 °C/min) for 12 h in a muffle furnace (L3/11/B410, Nabertherm GmbH, Lilienthal, Germany), followed by natural cooling. This temperature was chosen to minimize lithium loss and reduce excessive cation mixing that occurs at higher sintering temperatures [37,43].

The final products were carefully stored in vials in a desiccator. A sketch of the synthetic process is reported in Fig. 1.

The effect of pH during the co-precipitation process was also investigated. Besides samples obtained in uncontrolled natural conditions (pH < 1) where the precipitation pH is buffered by the oxalic acid/oxalate species in the solution, the precipitation of the mixed oxalate precursor was also carried out under a controlled pH = 6.5. Experiments at such an increased pH value were carried out with the objective of enhancing the precipitation of manganese and controlling the nucleation and growth [45,46]. Indeed, manganese oxalate is more soluble than nickel and cobalt oxalates, which can decrease the stoichiometric fraction of Mn in the precipitate compared to that found in the solution. Increasing pH can mitigate this effect. To maintain the pH at 6.5, controlled volumes of a 5.0 M sodium hydroxide solution (NaOH, Emsure Supelco, Merck, Darmstadt, Germany) were added to the precipitation media. The preparation of the Cu-doped NMC was obtained by adding weighted amounts of $CuSO_4$ (Anhydrous 98 %, Thermo Scientific, MA, USA) into the metal sulphate solution. All the synthetized samples are reported in Table 1, indicating the stoichiometries, the nominal concentration of the Cu impurities and the mixed oxalate precipitation pH.

Table 1
A summary of the samples synthesized and their synthetic methods.

Nominal Stochiometry	pH	Cu add ($\%_{at}$)	Sample ID
$LiNi_{0.8}Co_{0.1}Mn_{0.1}O_2$	Not controlled (<1)	0	NMC
$LiNi_{0.8}Co_{0.1}Mn_{0.1}O_2$	Controlled at 6.5	0	NMC_pH
$LiNi_{0.8}Co_{0.1}Mn_{0.1}Cu_{0.0066}O_2$	Not controlled (<1)	0.66	NMC_Cu(−)
$LiNi_{0.8}Co_{0.1}Mn_{0.1}Cu_{0.0109}O_2$	Not controlled (<1)	1.09	NMC_Cu(+)
$LiNi_{0.8}Co_{0.1}Mn_{0.1}Cu_{0.0066}O_2$	Controlled at 6.5	0.66	NMC_pH_Cu (−)
$LiNi_{0.8}Co_{0.1}Mn_{0.1}Cu_{0.0109}O_2$	Controlled at 6.5	1.09	NMC_pH_Cu (+)

2.2. Materials characterization

The chemical composition of all samples was determined by mineralization of the solids in acid solution and successive analyses of the resulting solutions by an Inductively Coupled Plasma–Optical Emission Spectrophotometer (ICP-OES, Avio 220 Max, Perkin Elmer). Mineralization of the powders was performed using 0.045 g of solid; these were placed in a 50 mL flask into which 4 mL of hydrochloric acid (37%ww, VWR Chemicals, Radnor, PA, USA) 4 mL of nitric acid (65%ww, VWR Chemicals, Radnor, PA, USA), and 2 mL of hydrogen peroxide solution (30%ww, Merck, Darmstadt, Germany) were added. The samples were subjected to magnetic stirring at a temperature of approximately 100 °C for 1 h. The phase composition of samples and their structural features were investigated by using X-ray diffraction (XRD) analysis with Cu Kα radiation (λ = 1.5406°A, 45 kV, 40 mA) within the 2θ range from 10° to 90° on Philips X'Pert PRO diffractometer. Attenuated total reflectance Fast-Fourier infrared spectroscopy (ATR-FTIR, Bruker LUMOS II) and Raman microspectroscopy (DILOR LabRam confocal micro-Raman using a 632 nm He—Ne laser) were employed to investigate the vibrational properties of materials. In addition, X-ray photoelectron spectroscopy (XPS) measurements were carried out to determine the chemical composition at the surface of the sample particles. A Specs XPS system with mono-chromatized Al Kα radiation (200 W, 12 kV) and a Phoibos 150 energy analyser (pass energy of 30 eV for the detail measurements) was used. To avoid surface contamination, the samples were transferred in inert gas atmosphere to the sample load lock of the XPS system. The peak fit of the XPS results was done with CasaXPS, using Shirley-type backgrounds and Gaussian-Lorentzian (GL30) peak shapes. All binding energies were calibrated to the main C1s peak at 284.8 eV.

Thermo-Gravimetric Analyses (TGA) were performed using a Mettler Toledo TGA/SDTA 850. TGA tests were performed in air flow (gas flow of 60 mL/min) between 25 °C–900 °C with a heating rate of 10 °C/min. High resolution-Field emission scanning electron microscopy (FESEM, Auriga Zeiss) was employed to observe the morphology of the cathode particles. Moreover, Energy-dispersive X-ray (EDX) spectroscopy experiments have been carried out during SEM acquisition. Particle size analysis was carried out using a laser diffraction particle size analyser (Mastersizer 3000, Malvern).

2.3. Electrochemical measurements

The electrode formulation and manufacturing were carried out in a dry-room with Dewpoint at −70 °C. The active material was mixed with carbon black (Super-P, Timcal) and polyvinylidene fluoride (PVDF, Solef) in a weight ratio of 8:1:1. Then, a suitable amount of N-Methyl-2-Pyrrolidone (NMP, Sigma-Aldrich) solution was added dropwise to evenly disperse the mixture, which was then coated onto an aluminum

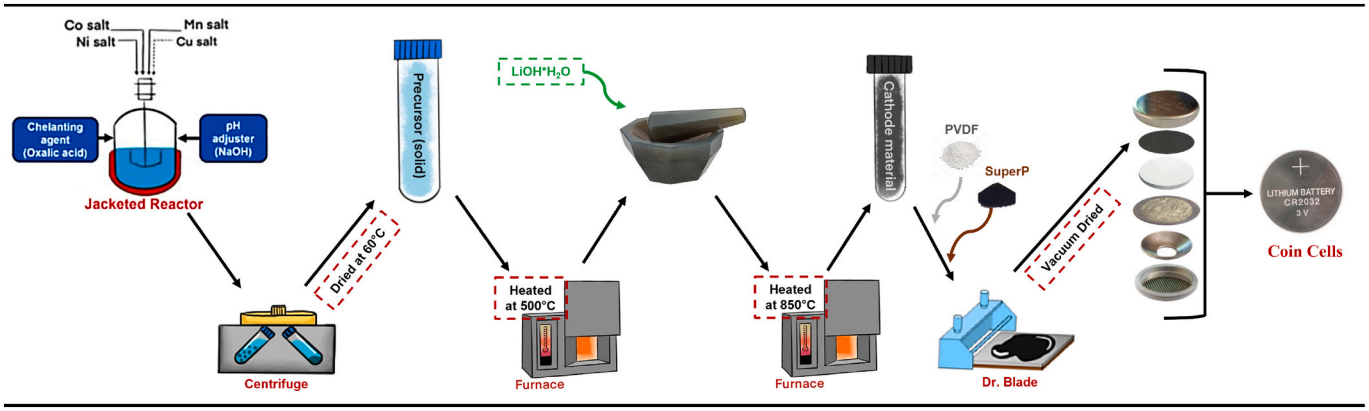

Fig. 1. Schematic diagram of the $LiNi_{0.8}Co_{0.1}Mn_{0.1}O_2$ preparation process via co-precipitation of the oxalic precursor in a jacketed reactor. The powder was then filtered, washed several times, and the obtained precursor was calcined in multiple steps, as detailed in the text. Successfully, the final powders were used to fabricate electrode films, which were cut into discs. These latter were used for electrochemical testing in coin cells.

foil by a doctor-blade (for a thickness controlled at 200 μm) and subsequently dried in a vacuum oven at 120 °C for 3 h to obtain the electrode film. The film was then Cut into discs with a diameter of 10 mm and dried again into a vacuum oven (Buchi tube) at 110 °C for 24 h and stored into an argon-filled glovebox (Mbraun LABstar pro). A Whatman glass fiber membrane (GF/A) was used as the separator to assemble the coin cells in the glove box for the electrochemical tests. The used electrolyte was a mixture of 1:1 vol% ethylene carbonate (EC) and dimethyl carbonate (DMC), with a concentration of 1.0 M lithium hexafluorophosphate ($LiPF_6$, Sigma-Aldrich). The electrolyte loading into the coin cells was ≈100 μL cm^{-2}. Coin cells (type 2032) were assembled by using a lithium disk with a diameter of 10 mm as the counter electrode. The final cell formulation is Li|$LiPF_6$,1.0 M in EC/DMC|NMC.

A NEWARE BTS 300 battery testing system was used to evaluate the rate capability and cycling performance at 3.0 to 4.3 V (vs Li/Li^+) at 30 °C for 100 cycles at C/10 (1C = 200 mA).

VSP Bio-Logic instrument was used to perform Ciclic Voltammetries (CVs) and Electrochemical Impedance Spectroscopy (EIS). CVs were acquired at different scan rate between 3 and 4.3 V. For EIS, the frequency range was set to 100 KHz–10 mHz with a signal amplitude of 10 mV.

3. Results and discussion

3.1. Characterization

The chemical compositions of the NMC811 samples obtained by ICP-OES are shown in Table 2 in which the nominal and the experimental values. All samples show a Ni:Mn:Co ratio very close to the nominal one, i.e. 8:1:1. A systematic Mn-loss is observed for all samples likely related to the slightly different solubility of the corresponding oxalate in comparison to the Ni and Co ones. For *NMC_(Cu-)*, *NMC_(Cu+)*, *NMC_pH_(Cu-)* and *NMC_pH_(Cu+)* samples, the atomic content of Cu incorporated into the layered oxide has been also quantified (see Table 2) highlighting a systematic smaller experimental value compared to the nominal one. These results point to selective Cu loss due to the solubility of copper oxalate: apparently Cu^{2+} ions are not completely precipitated from the precursors solution similarly to the Mn.

Turning to the impact of pH on the precipitation of the mixed metallic oxalate precursor, the ICP-OES data show that buffering the pH at 6.5 leads to an increase in Mn content: this provides indirect evidence of the expected promotion of manganese oxalate precipitation (approximately +14 %) [47]. On the other hand, the control of pH at 6.5 also slightly limits the incorporation of copper ions in the final NMC811 materials. One may speculate about the possible formation of a Cu^{2+}-oxalate coordination complex at pH = 6.5 that reduces its incorporation in the insoluble precipitate.

The effects of Cu^{2+} ions on the crystal structure of layered NMC811 cathode particles were investigated by XRD. As shown in Fig. 2a, for all the prepared cathode samples, strong diffraction peaks are observed in the XRD pattern from 10° to 90°, corresponding to the expected peaks of the trigonal α-$NaFeO_2$ structure ($R\bar{3}m$ space group) [48–51]. Additional small peaks are observed in the 20–35° range (see Fig. 2b), which can be attributed to the presence of impurities, like lithium carbonate (Li_2CO_3), sodium sulfate (Na_2SO_4), and lithium sulfate (Li_2SO_4). These sulfates originate from the precursors used during co-precipitation. Specifically, at a pH of 6.5, sodium from NaOH is introduced to control the pH, which may lead to the formation of Na_2SO_4. In fact, sodium sulfate is found only in pH-controlled materials. Moreover, these materials show a higher tendency for lithium to form lithium carbonate, suggesting that increasing the precipitation pH results in a higher content of this carbonate impurity. In contrast, the material without pH control mainly contains Li_2SO_4, with a lower amount of lithium carbonate.

The formation of residual lithium compounds (RLCs) is one of the most important problems of Ni-rich cathode materials [52–56], as it causes a loss of Li^+ ions and reduces capacity. This reduction is due to a carbonate layer on the surface that hinders Li^+ ion diffusion.

Remarkably, the presence of copper impurities does not result in the formation of copper oxide or other copper-related compounds, indicating that copper is likely incorporated into the cathode structure. These findings are consistent with previous evidence reported in the literature [30,57–59] and confirm that the overall layered structure is retained. Due to the comparable size of Cu^{2+} with Ni^{2+}, Co^{3+} and Mn^{4+}, these metals randomly occupy the same atomic site in the crystal lattice whereas the occupation of the Li^+ site is unlikely [30].

In the inset of Fig. 2a we also show a magnification of the diffraction peak assigned to the (003) plane of the trigonal phase. This peak shifts toward lower angles for samples prepared at pH = 6.5 as well as for Cu-doped samples, thus suggesting an expansion of the *c*-axis of the lattice [60]. Generally speaking, an anisotropic distortion of the layered lattice in the c-direction promotes a greater diffusivity of lithium ions during charge and discharge in cells and improves the capacity and stability of materials [56,61]. To confirm this expansion, Rietveld refinement was performed on all the samples, with the results reported in Table S2 and Fig. S1. As shown, the introduction of Cu impurities leads to an expansion of the c-axis and an increase in the unit cell volume, likely due to the larger ionic radius of Cu compared to the other transition metals. Notably, the sample *NMC_pH_Cu(+)* exhibits the largest changes in these parameters.

The comparison of ATR-FTIR spectra of all samples is shown in the Fig. 2c to confirm the nature and extent of the surface contamination by carbonate [62]. All samples show four main bands at ≈ 850, 1100, 1410 and 1470 cm^{-1}. The bands at 850, 1410 and 1470 cm^{-1} confirms the presence of lithium carbonate (i.e. CO_3^{2-} symmetric and asymmetric stretching vibrations centred around 1410 and 1470 cm^{-1} respectively, and out-of-plane vibrations at 850 cm^{-1}) [62–65]. The broadband at 1100 cm^{-1} is due to the residual sulphate moieties [66], possibly originating from the synthesis, as already seen in the XRD analysis [67]. Overall, the ATR-FTIR spectra of the various samples are very similar showing no changes between the different materials related to the impact of the pH or the copper content. The Raman investigation of samples is shown in the Fig. 2d to provide further information on local structure [68]. All Raman spectra reveal two main strong bands around 540 and 1000 cm^{-1}. The most intense band at 540 cm^{-1} is related to the transition metal-oxygen vibrations of the NMC811 oxide lattice [54]. The peak exhibits significant broadening, due to the mixing of the three transition metals. In particular, it consists of the overlap of specific vibrations of the Ni—O, Mn—O, and Co—O bonds in the variable surrounding coordination environments [69,70].

According to analysis done by Roland Jung et al. [70], at around

Table 2
Metal Element Atomic Percentages derived from ICP-OES for different NMC811 samples. Comparison between nominal and experimental stoichiometry.

Sample ID	Nominal stoichiometry	Experimental stoichiometry
NMC	$Li_{1.00}Ni_{0.8}Co_{0.1}Mn_{0.1}O_2$	$Li_{1.00}Ni_{0.82}Co_{0.11}Mn_{0.07}O_2$
NMC_pH	$Li_{1.00}Ni_{0.8}Co_{0.1}Mn_{0.1}O_2$	$Li_{1.03}Ni_{0.78}Co_{0.11}Mn_{0.08}O_2$
NMC_Cu(−)	$Li_{1.00}Ni_{0.8}Co_{0.1}Mn_{0.1}Cu_{0.0065}O_2$	$Li_{1.01}Ni_{0.80}Co_{0.11}Mn_{0.07}Cu_{0.0054}O_2$
NMC_Cu(+)	$Li_{1.00}Ni_{0.8}Co_{0.1}Mn_{0.1}Cu_{0.0109}O_2$	$Li_{1.00}Ni_{0.81}Co_{0.12}Mn_{0.07}Cu_{0.0089}O_2$
NMC_pH_Cu(−)	$Li_{1.00}Ni_{0.8}Co_{0.1}Mn_{0.1}Cu_{0.0065}O_2$	$Li_{1.04}Ni_{0.77}Co_{0.10}Mn_{0.08}Cu_{0.0040}O_2$
NMC_pH_Cu(+)	$Li_{1.00}Ni_{0.8}Co_{0.1}Mn_{0.1}Cu_{0.0109}O_2$	$Li_{1.05}Ni_{0.76}Co_{0.11}Mn_{0.08}Cu_{0.0064}O_2$

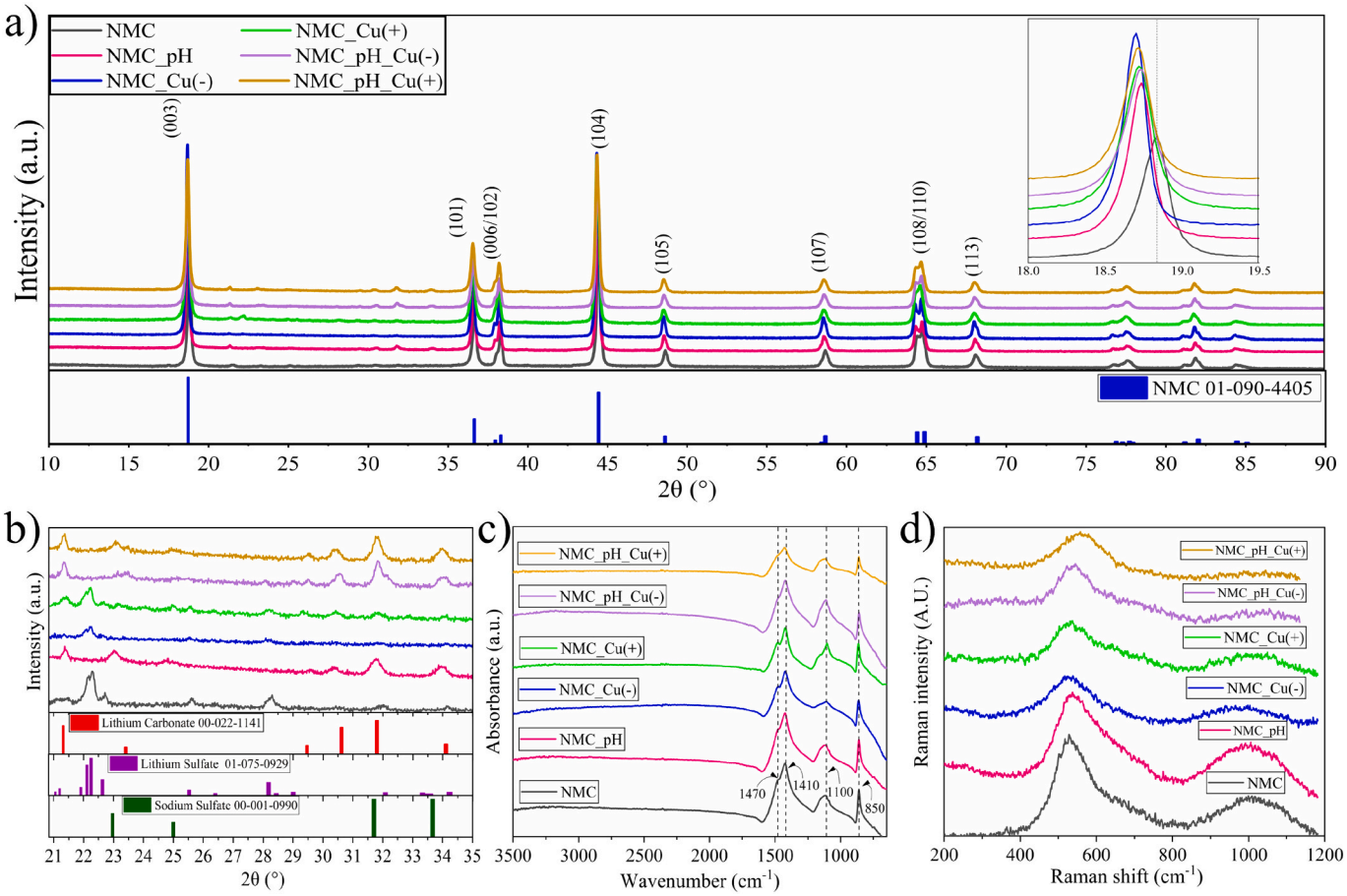

Fig. 2. (a) XRD patterns of the prepared cathode samples and the magnified (003) peak from 18.0° to 19.5°. Reference NMC811 (blue navy) is reported for comparison. (b) Magnified patterns in the range between 20 and 35° to detect impurity phases in the cathode samples; lithium carbonate (red line), lithium sulfate (purple line) and sodium sulfate (dark green line) were reported as reference. (c) FTIR-ATR patterns of the prepared cathode samples. (d) Raman spectra of the prepared cathode samples. (For interpretation of the references to colour in this figure legend, the reader is referred to the web version of this article.)

1000 cm^{-1}, NMC811 can show a broad band related to the metallic carbonates Li_2CO_3, $NiCO_3$, $CoCO_3$, and $MnCO_3$. Our observation is in line with the literature confirming with a third independent analysis the presence of inorganic carbonates on the surface of all samples [70,71].

The elemental composition and chemical state of the elements in the surface layer of the NMC811 particles was studied by XPS measurements, the results of the quantitative analysis are compiled in Table S3 and relevant detail spectra are displayed in Fig. S2-S5. Starting with the results of the quantitative analysis (Table S3), Cu could only be detected for the samples *NMC_pH_Cu(−)* and *NMC_pH_Cu(+)*. In case of the samples *NMC_Cu(−)* and *NMC_Cu(+)*, the Cu concentration was below the detection limit, which can be estimated to be ~0.02–0.03 at.% under the applied measurement conditions. As seen before, the surface of the NMC particles of these two samples was covered by a comparatively thicker layer of carbonaceous species which reduces the signal from the NMC material, as indicated by increased C contribution and significantly lower Ni, Mn, and Co concentrations. Significant concentrations of Na, in case of the materials which were prepared under pH control, and S could be detected for the samples originating from the precursors used during co-precipitation. Coming to the discussion of the detail spectra (Fig. S2-S5), due to the low Cu concentration only a weak peak is detected in the Cu 2p spectra (Fig. S4) of the samples *NMC_pH_(−)* and *NMC_pH_(+)* at 934.1 eV, a binding energy characteristic for Cu^{2+} species [72]. The analysis of the NMC transition metals (spectra in the Mn 2p, Co 2p and Ni 2p regions, Fig. S2) is complicated by multiplet splitting effects and overlap with Auger features [73], we therefore mainly discuss the shape and position of the spectra. All spectra reveal a slight shift to lower binding energies for the samples with pH control, which could indicate small changes of the oxidation state or the chemical structure. For example, the Ni $2p_{3/2}$ main peak is detected at ~855.3 eV for the samples with pH control (Fig. S4) and at ~855.6 eV for the samples without that. Similarly, a shift from ~780.3 to ~780.6 eV is observed for the Co $2p_{3/2}$ peak. The observed peak positions as well as the absence of the satellite feature at ~787 eV in the case of Co, point to an average oxidation state close to +3 for these two metals. The spectra in the Mn2p region contain a Ni Auger feature, which overlaps with the $Mn_{3/2}$ peak. As a consequence, the $Mn2p_{1/2}$ peak was used for comparison instead, which was detected for the pH samples at ~654.1 eV and for the others at ~654.5 eV. Taking into account the spin-orbit splitting of the Mn2p peak doublet (Δ = 11.7 eV), this translates to $Mn_{3/2}$ peak positions of 642.4 eV and 642.8, respectively; which points to an average oxidation state between Mn^{3+} and Mn^{4+}. The spectra in the Li 1 s region (Fig. S2-s4) and O 1 s spectra (Fig. S3-S5) confirm what seen with XRD, Raman and FTIR. Indeed, In Li 1 s, signals can be attributed to Li from NMC [74] Li_2CO_3, Li_2SO_4 while, in O 1 s spectra, we can find signals from Li_2O (528.3 eV), NMC (529.8 eV), O=C/carbonate species (531.6 eV, which also includes sulfate oxygen), and O—C species (533.2 eV).

The morphology of precursors and NMC-based materials have been studied by SEM-EDX. As shown in Fig. S6, the particles in all precursor samples display the typical spherical shape and they are composed of numerous primary nanosheets with different thicknesses and sizes, which are similar with those reported in the previous works [38,75,76]. However, the precursors synthesized at pH 6.5 display a more elongated

shape compared to those synthesized without pH control. This change in the morphology suggests that pH significantly influences the growth of secondary particles. In this context, primary particles refer to the nanosheets that directly form during nucleation, while secondary particles are larger, aggregated structures composed of these primary nanosheets.

The morphology of the cathode samples is displayed in Fig. 3. It is noted that, the prepared cathode active materials have an aggregated form of primary particles after calcination at 850 °C. Polygonal particles can be seen in the figure for all samples, which are formed by the reaction between the precursor and lithium hydroxide during the high temperature sintering process [60].

The distribution of atomic species in the NMC particles has been investigated by EDX mapping (Fig. S7): homogeneous distributions of Ni, Co, Mn and Cu can be observed. A quantitative characterization of the particles size has been performed by a particle size analyser for both the precursors and final NMC materials, as number and as volume distributions. The results of particle size analysis are shown in Fig. S8. Fig. S8a indicates that the precursor particles have similar sizes, suggesting that the presence of copper impurities and/or pH-controlled synthesis does not significantly influence their dimensions, as shown in the SEM images. After the calcination, a decrease of the particle size is observed. Overall, the sizes remain comparable among the series, as shown in Fig. S8b. Turning to the particle size distribution in terms of volume density (Figs. S8c and S8d), the precursor particles show two distinct peaks: one at 0.6 μm and another at 15 μm. The peak at 0.6 μm represents the majority of the particles, which are small in size and therefore occupy a minimal volume. While they have a high number density, they contribute only a small fraction to the total volume of the material, which is more relevant in terms of mass. This explains why they appear more prominently when analyzing the data based on number density (Fig. S8a), where the focus is on particle count rather than volume. In contrast, the peak at 15 μm corresponds to a smaller number of larger agglomerates that, despite their lower number density, contribute more significantly to the volume and mass of the material. Overall, the precursor particle sizes across different samples are similar, likely due to the consistent synthesis process. However, after calcination, particle agglomeration occurs, resulting in a more uneven distribution, as shown in Fig. S8d and detailed in Table S4. This suggests that the final cathodes contain agglomerates of varying sizes compared to the more uniform precursor particles. Table S4 reports the mode of particle size, calculated from measurements taken with the particle size analyser, for both the precursors and the final powders.

The mass variations from the TGA results for the samples is shown in the Fig. 4.

A slight initial mass change, indicated by *, is observed only in samples with a high copper concentration (*NMC_Cu(+)* and *NMC_pH_Cu (+)*). Unlike the other samples, these exhibit a slight weight gain, likely caused by the surface oxidation of copper. A second minor mass change occurs in all samples between 60 °C and approximately 150 °C, which can be attributed to dehydration reactions. Further weight losses, occurring at approximately 230 °C and 300 °C, are characteristic of the release of H_2O and CO_2. According to the literature [62], these changes are associated with the thermal decomposition of surface contaminants such as hydroxides, carbonates, and their hydrates. These surface contaminants may include compounds like $CoCO_3{\cdot}xH_2O$ and $MnCO_3{\cdot}xH_2O$, which can release H_2O and CO_2 at approximately 220 °C and 320 °C, respectively. Another possible contaminant is $NiCO_3{\cdot}2Ni(OH)_2{\cdot}xH_2O$, which exhibits one CO_2 weight loss at 250 °C and two H_2O weight losses at 125 °C and 300 °C. The final weight loss, observed in all samples at temperatures above 800 °C, corresponds to the thermal decomposition of the cathode material itself. Therefore, the thermal analysis confirms that the introduction of Cu does not affect the properties of the cathode materials.

3.2. Electrochemical performance of cathode electrodes

The impact of Cu impurities on the electrochemical performance of NMC811 cathode materials has been analysed by galvanostatic cycling tests as shown in the Fig. 5. The potential profiles obtained during the cycling are presented in Fig. S9. For all samples, the charge curves exhibit a pronounced slope between 3.6 V and 4.3 V vs. Li. This behaviour is primarily attributed to the oxidation of Ni^{2+} to Ni^{4+}, accompanied by the extraction of lithium ions [77]. The presence of this slope suggests that nickel redox reactions dominate the electrochemical behaviour of these materials. Instead, Cu^{2+} does not participate directly in the redox processes but it can influence the electrochemical behaviour [78,79]. Indeed, as shown in Table 3 and Fig. 5a, the discharge specific

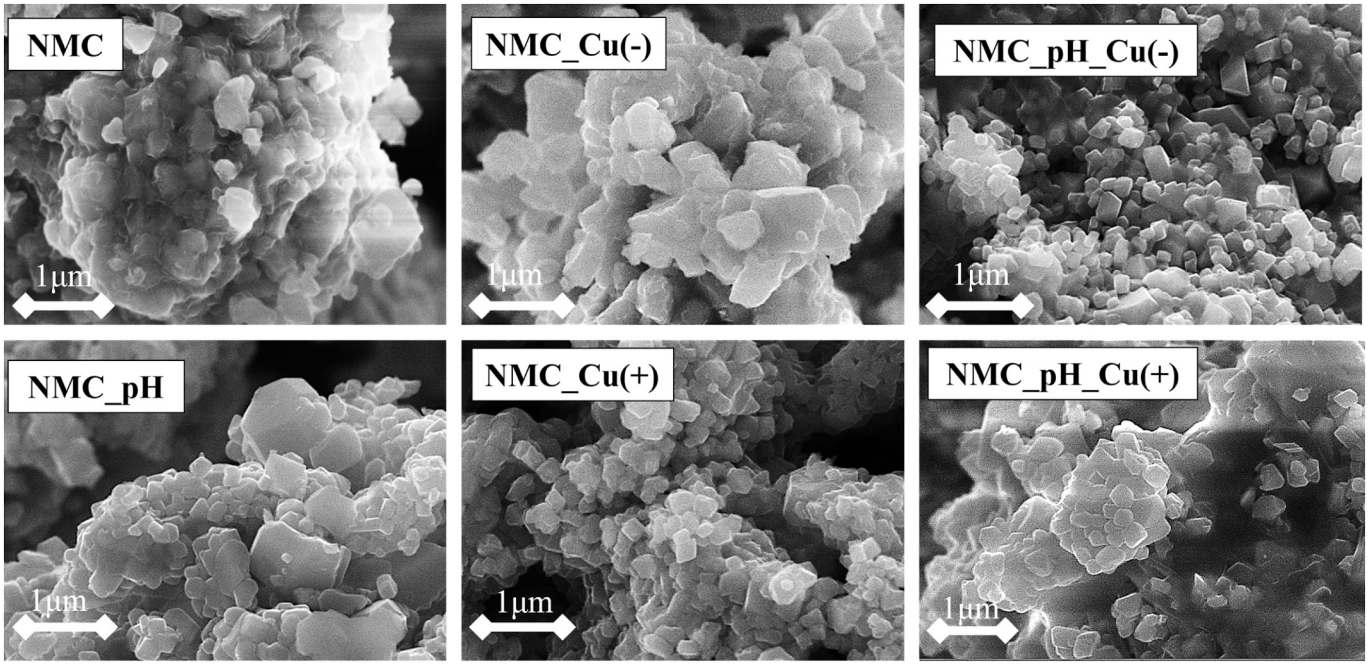

Fig. 3. SEM images of cathode material particles, with and without Cu impurities, acquired at x50K magnification.

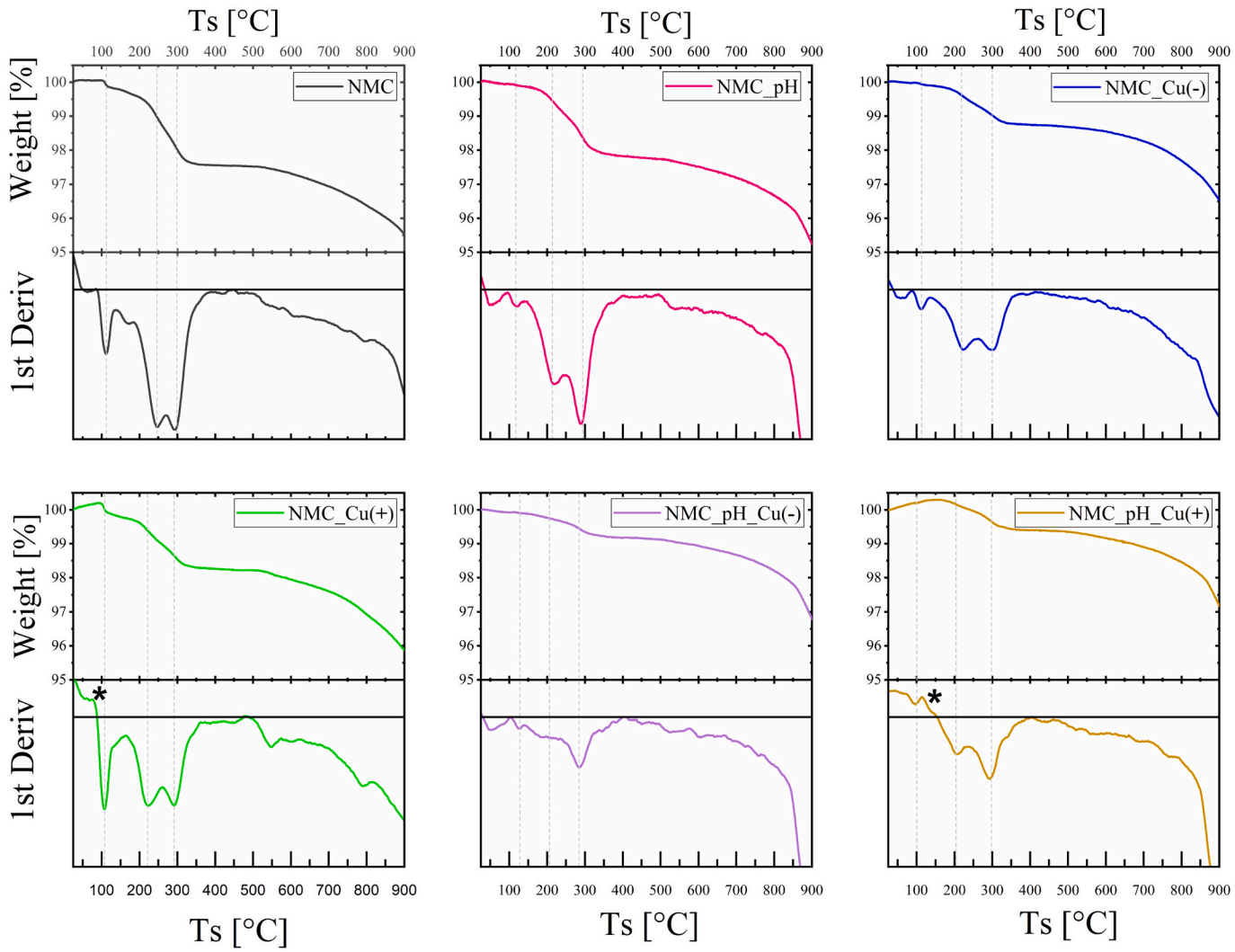

Fig. 4. TGA analysis under air of cathode material samples. For each sample the characteristic weight loss (upper panel) and the corresponding 1st derivate (lower panel) are shown for a 10 °C/min temperature ramp from 25 to 900 °C.

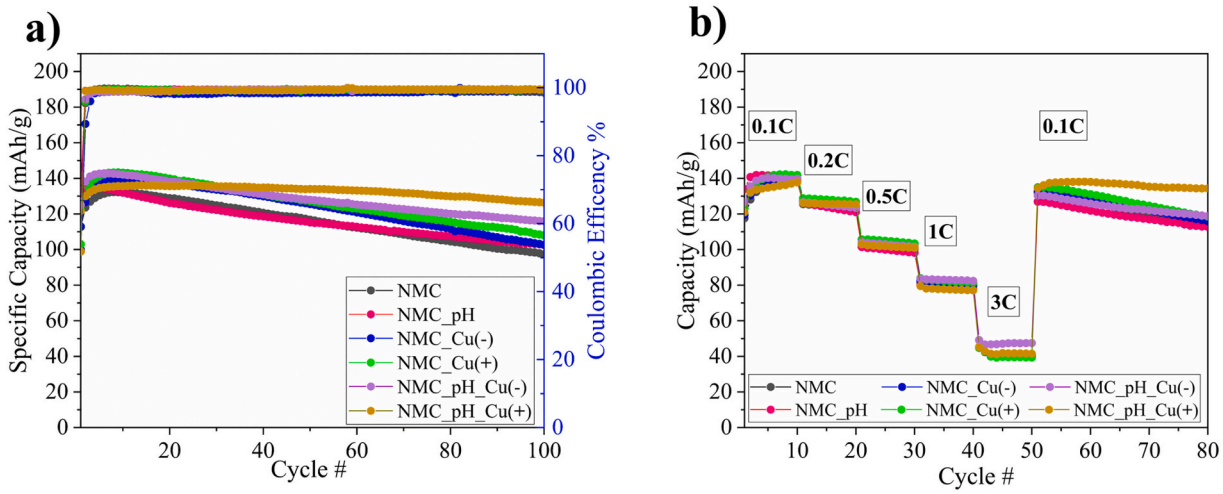

Fig. 5. (a) Specific capacity vs cycle number plot at 0.1C. (b) Rate capability performance of the electrodes from 0.1 to 3C. Theoretical specific capacity is 200 $mAhg^{-1}$. Lithium foil was used as counter electrode and the galvanostatic test was performed between 2 and 4.3 V.

Table 3
Measured specific discharge capacities in the 1st and 10th cycle and specific capacity retentions in all half-cells between the 10th and 50th/100th cycle at 0.1C. (results based on data from Fig. 5a).

Sample	Discharge Capacity at 1st cycle (mAh/g)	Discharge Capacity at 10th cycle (mAh/g)	Retention Rate at 50th cycle (%)	Retention Rate at 100th cycle (%)
NMC	112.71	131.90	88.49	73.76
NMC_pH	131.70	131.95	87.34	77.79
NMC_Cu(−)	112.91	138.67	90.54	74.02
NMC_Cu(+)	122.71	143.11	88.79	75.43
NMC_pH_Cu (−)	133.51	142.08	90.03	81.59
NMC_pH_Cu (+)	121.63	135.62	98.81	93.16

capacity after the first ten cycles is higher in Cu-doped materials compared to pristine cathode materials.

Overall, these features suggest that the presence of copper impurities partially improves the capacity. This effect is in line with previous studies as reported in Table S5 which compare pristine NMC samples with those containing varying atomic percentages of copper. These comparisons confirm that copper incorporation enhances capacity, possibly by facilitating lithium-ion extraction [32]. This improvement is likely due to an increased lithium diffusion coefficient, resulting from the expansion of the unit cell and the formation of more favourable particle structures. This effect is especially important because slow lithium-ion diffusion kinetics are a well-known limitation in high-capacity nickel-rich cathodes, leading to irreversible capacity loss during the first cycle [80].

The cycling performance of all cells shown in Fig. 5 highlight a gradual increase in specific discharge capacity during the first 10 cycles. This behaviour is possibly due to the partial decomposition of carbonate species that occurs in the early stages of cycling [70,75]. In particular, surface impurities can form a resistive film around the NMC811 particles, which must partially break down before delithiation can proceed. This phenomenon leads to an increased overpotential during the first charge/discharge cycles [70]. After a few cycles, the decomposition seems to disappear as seen from a decrease in the overpotential and in the calculated hysteresis. (Fig. S9 and Table S6). These results emphasize the need to optimize both synthesis methods and storage conditions. Storing the material in a dehumidified environment or potentially reducing the amount of lithium used during synthesis could be effective strategies to minimize surface impurities. This, in turn, would contribute to improving the materials electrochemical performance. After these initial cycles, all materials exhibit a slow and gradual decline in capacity, with the exception of *NMC_pH_Cu(+)*, which demonstrates exceptional stability compared to the other samples (Table 3 and Fig. 5a). The superior cycling stability of the *NMC_pH_Cu(+)* cathode can be attributed to its enhanced structural integrity. Therefore, despite the slight decrease in capacity, higher copper concentrations contribute to remarkable cycling stability. Furthermore, the Coulombic efficiency (Fig. 5a) shows that for all samples, the efficiency stabilizes after the first cycle, indicating that the charge and discharge processes are highly reversible. Moreover, to evaluate the impact of copper incorporation on battery longevity over hundreds of cycles, long-term cycling data are presented in Fig. S10. Despite the typical decline in specific capacity observed in Ni-rich cathodes, the cathodes with Cu impurities retain their specific capacity more effectively than the NMC sample after 300 cycles, confirming the beneficial effect of Cu in mitigating the cathode degradation process.

Rate capability tests were performed at various current rates: 0.1C, 0.2C, 0.5C, 1.0C, and 3.0C, with 1C corresponding to 200 mAh/g. All samples exhibited similar electrochemical behaviour, showing close performance across different current densities. Notably, when the current was returned to 0.1C after cycling at higher rates, the electrodes recovered nearly all their initial discharge capacity. The *NMC_pH_Cu(+)* cathode, in particular, delivered a specific capacity of 134.46 mAh/g upon returning to 0.1C, fully recovering its specific capacity and demonstrating outstanding stability over 80 cycles.

To confirm the idea that Cu could enhance the capacity by the increase in the lithium diffusion coefficient, cyclic voltammetries at different scan rates were performed to investigate the lithium diffusion coefficient for all the materials. The results are presented in Fig. S11-S12 and Table S7. Both pH and copper impurities were found to influence the diffusion coefficient in a similar way, leading to an increase compared to pristine NMC. Notably, the materials with copper exhibited the highest diffusion coefficients, consistent with the trends observed in the galvanostatic cycling and rate capability tests. Therefore, the samples synthesized with controlled pH and Cu impurities exhibited the highest values. Overall, these findings may help explain the improved capacity observed in copper-doped materials compared to NMC and NMC_pH. After the CV experiments, we also performed EIS analysis to investigate the solid electrolyte interface (SEI) formation and charge transfer resistance. Fig. S13 shows the results, where only one depressed semicircle can be observed for the samples. To determine whether the semicircle is related to ionic motion across the Cathode Electrolyte Interface (R_{CEI}) or to the charge-transfer phenomena (R_{CT}), we considered the frequency at the maximum of the semicircle. From the Table S8, the frequencies are all greater than several hundred ohms and, as reported in many articles [81,82], they are correlated with charge transfer phenomena (10–1000 Hz), which is also confirmed by the calculated time constant. This allows us to calculate the charge transfer resistance, which is 426, 356, 363, 372, 318, and 292 Ω, respectively, for *NMC, NMC_pH, NMC_Cu(−), NMC_Cu(+), NMC_pH_Cu(−), and NMC_pH_Cu (+)*. These results confirm the beneficial effect of Cu impurities on charge transfer properties.

Finally, post-mortem SEM images were acquired for *NMC* and *NMC_pH_Cu(+)* to investigate the effect of copper impurities on the formation of microcracks. Fig. S14 shows the two materials before and after cycling, revealing how *NMC_pH_Cu(+)* exhibits fewer visible microcracks in the cross-sectional images compared to pristine *NMC*, suggesting that copper doping helps mitigate the formation of microfractures during cycling.

4. Conclusions

This study investigated the influence of copper (Cu^{2+}) impurities on the crystal structure and electrochemical performance of NMC811 cathode materials. Cu^{2+} impurities were carefully introduced via an oxalate co-precipitation process to simulate concentrations typically found during the hydrometallurgical resynthesis of cathode materials from end-of-life batteries.

The results demonstrate that Cu^{2+} is incorporated into the crystal lattice without forming separate oxide phases, leading to an expansion of the c-parameter and a reduction in cation mixing. These structural changes could improve lithium-ion diffusion and enhance the electrochemical stability of the material.

Electrochemical tests revealed that Cu-doped samples exhibited higher initial specific capacity and improved cycling stability compared to pristine NMC811. In particular, the *NMC_pH_Cu(+)* sample showed an outstanding cycling stability, with a capacity retention of 93 % after 100 cycles. These findings suggest that Cu impurities, instead of being detrimental, can act like a dopant, enhancing material properties under controlled conditions. Indeed, *NMC_pH_Cu(+)* shows better lithium diffusion coefficient, charge transfer resistance and less microcracks after cycling.

In addition to NMC811, the results of this study are applicable to a variety of other cathode materials and stoichiometries. The observed contamination levels in the recycled materials allow for the re-synthesis of different cathode materials, thereby increasing the flexibility and applicability of our approach in the broader battery recycling sector.

This work underscores the potential for utilizing these findings in the recycling of a wide range of battery chemistries. Future studies should explore the effects of multiple impurities, such as Fe and Al, simultaneously introduced into the same material to understand their combined interactions and potential synergies. Moreover, Cu impurities and Cu-induced local defects can be tolerated or controlled via crystallization pathways, processing conditions and thermal treatment.

These approachs would provide deeper insights into optimizing recycled cathode materials and reducing purification costs, thereby advancing sustainable recycling strategies for lithium-ion batteries.

CRediT authorship contribution statement

Antonino Giarrizzo: Writing – original draft, Investigation. **Arcangelo Celeste:** Writing – original draft, Methodology, Investigation, Data curation. **Marco Agostini:** Writing – review & editing, Methodology. **Pier Giorgio Schiavi:** Writing – review & editing, Methodology. **Graziano Di Donato:** Investigation, Formal analysis. **Thomas Diemant:** Investigation, Formal analysis. **Pietro Altimari:** Writing – review & editing, Methodology. **Micol Di Veroli:** Writing – review & editing. **Francesca Pagnanelli:** Writing – review & editing, Supervision, Methodology, Funding acquisition. **Sergio Brutti:** Writing – review & editing, Supervision, Methodology, Funding acquisition.

Declaration of competing interest

The authors declare that they have no known competing financial interests or personal relationships that could have appeared to influence the work reported in this paper.

Acknowledgments

The contribution of A. Celeste, S. Brutti and P. Altimari to this study was carried out within the NEST—Network for Energy Sustainable Transition and received funding from the European Union Next-Generation EU (PIANO NAZIONALE DI RIPRESA E RESILIENZA (PNRR)—MISSIONE 4 COMPONENTE 2, INVESTIMENTO 1.3—D.D. 1561 11/10/2022, B53C22004070006). This manuscript reflects only the authors' views and opinions, neither the European Union nor the European Commission can be considered responsible for them. All Sapienza staff within the NEST project participate to this action under the frame of the grant PE2421852F05911E. The research project here reported was supported by the “Centro Nazionale per la Mobilità Sostenibile (MOST) CN4 Spoke 13 Batterie e Trazione Elettrica” funded by the Italian Government and the European Union in the frame of the “Missione 4 Componente 2 Investimento 1.4 – Potenziamento strutture di ricerca e creazione di “campioni nazionali di R&S" su alcune Key Enabling Technologies del PNRR (Avviso MUR n.3138 del 16–12-2021)”.

Appendix A. Supplementary data

Supplementary data to this article can be found online at https://doi.org/10.1016/j.cej.2025.164686.

Data availability

Data will be made available on request.

References

[1] Matthew L. Wald, Wind drives growing use of batteries, New York Times (2010).
[2] D. Larcher, J.M. Tarascon, Towards greener and more sustainable batteries for electrical energy storage, Nat. Chem. 7 (2015) 19–29, https://doi.org/10.1038/nchem.2085.
[3] J. Neumann, M. Petranikova, M. Meeus, J.D. Gamarra, R. Younesi, M. Winter, S. Nowak, Recycling of lithium-ion batteries—current state of the art, circular economy, and next generation recycling, Adv. Energy Mater. 12 (2022) 2102917.
[4] R. Zhang, Z. Meng, X. Ma, M. Chen, B. Chen, Y. Zheng, Z. Yao, P. Vanaphuti, S. Bong, Z. Yang, Understanding fundamental effects of Cu impurity in different forms for recovered LiNi0. 6Co0. 2Mn0. 2O2 cathode materials, Nano Energy 78 (2020) 105214.
[5] R. Zhang, Y. Zheng, Z. Yao, P. Vanaphuti, X. Ma, S. Bong, M. Chen, Y. Liu, F. Cheng, Z. Yang, Systematic study of Al impurity for NCM622 cathode materials, ACS Sustain. Chem. Eng. 8 (2020) 9875–9884.
[6] E.C. of Auditors, The EU's industrial policy on batteries – New strategic impetus needed. Special report 15, 2023, Publications Office of the European Union, 2023. doi:doi/https://doi.org/10.2865/862094.
[7] K.E. Rosendahl, D.R. Rubiano, How effective is lithium recycling as a remedy for resource scarcity? Environ Resour Econ (Dordr) 74 (2019) 985–1010.
[8] J. Xiao, J. Li, Z. Xu, Recycling metals from lithium ion battery by mechanical separation and vacuum metallurgy, J. Hazard. Mater. 338 (2017) 124–131, https://doi.org/10.1016/j.jhazmat.2017.05.024.
[9] N.K. Arora, I. Mishra, United Nations sustainable development goals 2030 and environmental sustainability: race against time, Environ. Sustain. 2 (2019) 339–342.
[10] L. Carlsen, R. Bruggemann, The 17 United Nations' sustainable development goals: a status by 2020, Int. J. Sustain. Dev. World Ecol. 29 (2022) 219–229.
[11] Battery Regulation (EU) 2023, Regulation (EU) 2023/1542 of the European Parliament and of the Council of 12 July 2023 Concerning Batteries and Waste Batteries, Amending Directive 2008/98/EC and Regulation (EU) 2019/1020 and Repealing Directive 2006/66/EC. n.d. Available online: https://eur-lex.europa.eu/eli/reg/2023/1542/oj., (n.d.).
[12] Pratima Meshram, B.D. Pandey, T.R. Mankhand, Extraction of lithium from primary and secondary sources by pre-treatment, leaching and separation: a comprehensive review, Hydrometallurgy (2014) 192–208.
[13] Xianlai Zeng, Jinhui Li, Narendra Singh, Recycling of spent lithium-ion battery: a critical review, Environ. Sci. Technol. (2014) 1129–1165.
[14] M. Chen, X. Ma, B. Chen, R. Arsenault, P. Karlson, N. Simon, Y. Wang, Recycling end-of-life electric vehicle Lithium-ion batteries, Joule 3 (2019) 2622–2646, https://doi.org/10.1016/j.joule.2019.09.014.
[15] E.G. Pinna, M.C. Ruiz, M.W. Ojeda, M.H. Rodriguez, Cathodes of spent Li-ion batteries: dissolution with phosphoric acid and recovery of lithium and cobalt from leach liquors, Hydrometallurgy 167 (2017) 66–71, https://doi.org/10.1016/j.hydromet.2016.10.024.
[16] J. Hu, J. Zhang, H. Li, Y. Chen, C. Wang, A promising approach for the recovery of high value-added metals from spent lithium-ion batteries, J. Power Sources 351 (2017) 192–199.
[17] T. Georgi-Maschler, B. Friedrich, R. Weyhe, H. Heegn, M. Rutz, Development of a recycling process for Li-ion batteries, J. Power Sources 207 (2012) 173–182.
[18] M. Chen, Z. Zheng, Q. Wang, Y. Zhang, X. Ma, C. Shen, D. Xu, J. Liu, Y. Liu, P. Gionet, Closed loop recycling of electric vehicle batteries to enable ultra-high quality cathode powder, Sci. Rep. 9 (2019) 1654.
[19] X. Zhang, L. Li, E. Fan, Q. Xue, Y. Bian, F. Wu, R. Chen, Toward sustainable and systematic recycling of spent rechargeable batteries, Chem. Soc. Rev. 47 (2018) 7239–7302.
[20] A. Chagnes, B. Pospiech, A brief review on hydrometallurgical technologies for recycling spent lithium-ion batteries, J. Chem. Technol. Biotechnol. 88 (2013) 1191–1199.
[21] H. Wang, B. Friedrich, Development of a highly efficient hydrometallurgical recycling process for automotive Li–ion batteries, Journal of Sustainable Metallurgy 1 (2015) 168–178.
[22] P.G. Schiavi, M. Branchi, E. Casalese, P. Altimari, M.A. Navarra, F. Pagnanelli, Resynthesis of NMC111 cathodic material from real waste lithium ion batteries, Chem. Eng. Trans. 86 (2021) 463–468.
[23] F. Pagnanelli, P. Altimari, M. Colasanti, J. Coletta, L. D'Annibale, A. Mancini, O. Russina, P.G. Schiavi, Recycling Li-ion batteries via the re-synthesis route: improving the process sustainability by using Lithium Iron phosphate (LFP) scraps as reducing agents in the leaching operation, Metals (Basel) 14 (2024) 1275.
[24] S.G. Zhu, W.Z. He, Removal of organic impurities in lithium cobalt oxide from spent lithium ion batteries by ultrasonic irradiation, Adv. Mater. Res. 864 (2014) 1937–1940.
[25] F. Peng, D. Mu, R. Li, Y. Liu, Y. Ji, C. Dai, F. Ding, Impurity removal with highly selective and efficient methods and the recycling of transition metals from spent lithium-ion batteries, RSC Adv. 9 (2019) 21922–21930.
[26] S. Park, D. Kim, H. Ku, M. Jo, S. Kim, J. Song, J. Yu, K. Kwon, The effect of Fe as an impurity element for sustainable resynthesis of Li [Ni1/3Co1/3Mn1/3] O2 cathode material from spent lithium-ion batteries, Electrochim. Acta 296 (2019) 814–822.
[27] Sa, Q. Synthesis and impurity study of high performance LiNixMnyCozO2 cathode materials from lithium ion battery recovery stream. Worcester Polytechnic Institute, Massachusetts, 2015.
[28] C. Peng, K. Lahtinen, E. Medina, P. Kauranen, M. Karppinen, T. Kallio, B.P. Wilson, M. Lundström, Role of impurity copper in Li-ion battery recycling to LiCoO2 cathode materials, J. Power Sources 450 (2020) 227630.
[29] J. Ren, R. Li, Y. Liu, Y. Cheng, D. Mu, R. Zheng, J. Liu, C. Dai, The impact of aluminum impurity on the regenerated lithium nickel cobalt manganese oxide cathode materials from spent LIBs, New J. Chem. 41 (2017) 10959–10965, https://doi.org/10.1039/C7NJ01206C.
[30] Q. Sa, J.A. Heelan, Y. Lu, D. Apelian, Y. Wang, Copper impurity effects on LiNi1/3Mn1/3Co1/3O2 cathode material, ACS Appl. Mater. Interfaces 7 (2015) 20585–20590, https://doi.org/10.1021/acsami.5b04426.

[31] Y. Zhao, X. Yuan, L. Jiang, J. Wen, H. Wang, R. Guan, J. Zhang, G. Zeng, Regeneration and reutilization of cathode materials from spent lithium-ion batteries, Chem. Eng. J. 383 (2020), https://doi.org/10.1016/j.cej.2019.123089.

[32] C.P. Woodley, R.A. Cooper, B.M. Bartlett, Cu doping increases capacity retention in LiNi0.6Mn0.2Co0.2O2 (NMC622) by altering the potential of the Ni-based redox couple and inhibiting particle pulverization, ACS Appl Energy Mater 7 (2024) 7875–7884, https://doi.org/10.1021/acsaem.4c01450.

[33] Y. Lu, H. Jin, Y. Mo, Y. Qu, B. Du, Y. Chen, Synthesis and characterization of cu-doped LiNi0.6Co0.2Mn0.2O2 materials for Li-ion batteries, J. Alloys Compd. 844 (2020) 156180, https://doi.org/10.1016/j.jallcom.2020.156180.

[34] T. Wu, G. Wang, B. Liu, Q. Huang, Y. Su, F. Wu, R.M. Kelly, The role of cu impurity on the structure and electrochemical performance of Ni-rich cathode material for lithium-ion batteries, J. Power Sources 494 (2021) 229774, https://doi.org/10.1016/j.jpowsour.2021.229774.

[35] Meng, Z., Ma, X., Hou, J., Zheng, Y., Wang, Y. Impurity impacts of recycling NMC cathodes, Adv. Energy Mater. (n.d.) 2405383.

[36] LIFE DRONE Project: Direct PROduction of New Electrode Materials (ENV/IT/000520) (www.lifedrone.eu) from Battery Recycling, (n.d.).

[37] M. Malik, K.H. Chan, G. Azimi, Review on the synthesis of LiNixMnyCo1-x-yO2 (NMC) cathodes for lithium-ion batteries, Mater Today Energy 28 (2022), https://doi.org/10.1016/j.mtener.2022.101066.

[38] X. Yao, Z. Xu, Z. Yao, W. Cheng, H. Gao, Q. Zhao, J. Li, A. Zhou, Oxalate co-precipitation synthesis of LiNi 0.6 co 0.2 Mn 0.2 O 2 for low-cost and high-energy lithium-ion batteries, Mater Today Commun 19 (2019) 262–270, https://doi.org/10.1016/j.mtcomm.2019.02.001.

[39] G.M. Koenig Jr., I. Belharouak, H. Deng, Y.-K. Sun, K. Amine, Composition-tailored synthesis of gradient transition metal precursor particles for lithium-ion battery cathode materials, Chem. Mater. 23 (2011) 1954–1963.

[40] H. Dong, E. Gardner, A.F. Barron, G.M. Koenig Jr., Apparent activation energy of multicomponent transition metal oxalates to probe synthesis of battery precursor materials, Powder Technol. 354 (2019) 158–164.

[41] J.-Z. Kong, X.-Y. Yang, H.-F. Zhai, C. Ren, H. Li, J.-X. Li, Z. Tang, F. Zhou, Synthesis and electrochemical properties of Li-excess Li1+ x [Ni0. 5Co0. 2Mn0. 3] O2 cathode materials using ammonia-free chelating agent, J. Alloys Compd. 580 (2013) 491–496.

[42] X. Luo, X. Wang, L. Liao, X. Wang, S. Gamboa, P.J. Sebastian, Effects of synthesis conditions on the structural and electrochemical properties of layered Li [Ni1/3Co1/3Mn1/3] O2 cathode material via the hydroxide co-precipitation method LIB SCITECH, J. Power Sources 161 (2006) 601–605.

[43] T. Wang, K. Ren, M. He, W. Dong, W. Xiao, H. Pan, J. Yang, Y. Yang, P. Liu, Z. Cao, Synthesis and manipulation of single-crystalline lithium nickel manganese cobalt oxide cathodes: a review of growth mechanism, Front. Chem. 8 (2020) 747.

[44] S. Yang, X. Wang, X. Yang, L. Liu, Z. Liu, Y. Bai, Y. Wang, Influence of Li source on tap density and high rate cycling performance of spherical Li [NiCoMn] O for advanced lithium-ion batteries, J. Solid State Electrochem. 16 (2012).

[45] Y. Zhang, H. Cao, J. Zhang, B. Xia, Synthesis of LiNi0. 6Co0. 2Mn0. 2O2 cathode material by a carbonate co-precipitation method and its electrochemical characterization, Solid State Ionics 177 (2006) 3303–3307.

[46] M. Noh, J. Cho, Optimized synthetic conditions of LiNi0. 5Co0. 2Mn0. 3O2 cathode materials for high rate lithium batteries via co-precipitation method, J. Electrochem. Soc. 160 (2012) A105.

[47] T.R. Penki, D. Shanmughasundaram, N. Munichandraiah, Porous lithium rich Li1. 2Mn0. 54Ni0. 22Fe0. 04O2prepared by microemulsion route as a high capacity and high rate capability positive electrode material, Electrochim. Acta 143 (2014) 152–160.

[48] C. Giacovazzo, Fundamentals of crystallography, Oxford university press, USA, 2002.

[49] C.-H. Jo, D.-H. Cho, H.-J. Noh, H. Yashiro, Y.-K. Sun, S.T. Myung, An effective method to reduce residual lithium compounds on Ni-rich Li [Ni 0.6 co 0.2 Mn 0.2] O 2 active material using a phosphoric acid derived Li 3 PO 4 nanolayer, Nano Res. 8 (2015) 1464–1479.

[50] L. Silvestri, A. Celeste, M. Tuccillo, S. Brutti, Li-rich layered oxides: structure and doping strategies to enable co-poor/co-free cathodes for Li-ion batteries, Crystals (Basel) 13 (2023) 204.

[51] W. Liu, X. Li, D. Xiong, Y. Hao, J. Li, H. Kou, B. Yan, D. Li, S. Lu, A. Koo, Significantly improving cycling performance of cathodes in lithium ion batteries: the effect of Al2O3 and LiAlO2 coatings on LiNi0. 6Co0. 2Mn0. 2O2, Nano Energy 44 (2018) 111–120.

[52] S.S. Zhang, Understanding of performance degradation of LiNi0. 80Co0. 10Mn0. 10O2 cathode material operating at high potentials, J. Energy Chem. 41 (2020) 135–141.

[53] D.-H. Cho, C.-H. Jo, W. Cho, Y.-J. Kim, H. Yashiro, Y.-K. Sun, S.-T. Myung, Effect of residual lithium compounds on layer Ni-rich Li [Ni0. 7Mn0. 3] O2, J. Electrochem. Soc. 161 (2014) A920.

[54] E. Floresa, P. Nováka, U. Aschauerb, E.J. Berga, Cation ordering and redox chemistry of layered Ni-rich NCMs: an operando Raman spectroscopy study, Chem. Mater. 32 (1) (2020) 186–194, https://doi.org/10.1021/acs.chemmater.9b03202.

[55] J.H. Jo, C.-H. Jo, H. Yashiro, S.-J. Kim, S.-T. Myung, Re-heating effect of Ni-rich cathode material on structure and electrochemical properties, J. Power Sources 313 (2016) 1–8.

[56] G.V. Zhuang, G. Chen, J. Shim, X. Song, P.N. Ross, T.J. Richardson, Li2CO3 in LiNi0.8Co0.15Al0.05O2 cathodes and its effects on capacity and power, J. Power Sources 134 (2) (2004) 293–297.

[57] S. Ye, Y. Xia, P. Zhang, Z. Qiao, Al, B, and F doped LiNi 1/3 co 1/3 Mn 1/3 O 2 as cathode material of lithium-ion batteries, J. Solid State Electrochem. 11 (2007) 805–810.

[58] D. Liu, Z. Wang, L. Chen, Comparison of structure and electrochemistry of Al-and Fe-doped LiNi1/3Co1/3Mn1/3O2, Electrochim. Acta 51 (2006) 4199–4203.

[59] Y. Ding, P. Zhang, Y. Jiang, D. Gao, Effect of rare earth elements doping on structure and electrochemical properties of LiNi1/3Co1/3Mn1/3O2 for lithium-ion battery, Solid State Ionics 178 (2007) 967–971.

[60] L. Liang, K. Du, Z. Peng, Y. Cao, J. Duan, J. Jiang, G. Hu, Co-precipitation synthesis of Ni0.6Co0.2Mn 0.2(OH)2 precursor and characterization of LiNi 0.6Co0.2Mn0.2O2 cathode material for secondary lithium batteries, Electrochim. Acta 130 (2014) 82–89, https://doi.org/10.1016/j.electacta.2014.02.100.

[61] Y.W. Denis, K. Yanagida, Structural analysis of Li2MnO3 and related Li-Mn-O materials, J. Electrochem. Soc. 158 (2011) A1015.

[62] J. Sicklinger, M. Metzger, H. Beyer, D. Pritzl, H.A. Gasteiger, Ambient storage derived surface contamination of NCM811 and NCM111: performance implications and mitigation strategies, J. Electrochem. Soc. 166 (2019) A2322–A2335.

[63] P. Pasierb, S. Komornicki, M. Rokita, M. Rękas, Structural properties of Li2CO3–BaCO3 system derived from IR and Raman spectroscopy, J. Mol. Struct. 596 (2001) 151–156.

[64] W.-L. Wang, H. Jiang, Z. Liu, X. Liu, Effects of base concentration and cation on hydrothermal processes of cetyltrimethylammonium permanganate in various aqueous media, J. Mater. Chem. 15 (2005) 1002–1010.

[65] S. Meini, N. Tsiouvaras, K.U. Schwenke, M. Piana, H. Beyer, L. Lange, H. A. Gasteiger, Rechargeability of Li-air cathodes pre-filled with discharge products using an ether-based electrolyte solution: implications for cycle-life of Li-air cells, Phys. Chem. Chem. Phys. 15 (2013) 11478–11493, https://doi.org/10.1039/c3cp51112j.

[66] A.C. Martinez, S. Grugeon, D. Cailleu, M. Courty, P. Tran-Van, B. Delobel, S. Laruelle, High reactivity of the nickel-rich LiNi1-x-yMnxCoyO2 layered materials surface towards H2O/CO2 atmosphere and LiPF6-based electrolyte, J. Power Sources 468 (2020) 228204, https://doi.org/10.1016/j.jpowsour.2020.228204.

[67] R.M. Silverstein, G.C. Bassler, Spectrometric identification of organic compounds, J. Chem. Educ. 39 (1962) 546.

[68] M.M.S. Sanad, N.K. Meselhy, H.A. El-Boraey, A. Toghan, Controllable engineering of new ZnAl2O4-decorated LiNi0·8Mn0·1Co0·1O2 cathode materials for high performance lithium-ion batteries, J. Mater. Res. Technol. 23 (2023) 1528–1542, https://doi.org/10.1016/j.jmrt.2023.01.102.

[69] Kerlau, M., Marcinek, M., Srinivasan, V., Kostecki, R. M. Reprint of Studies of local degradation phenomena in composite cathodes for lithium-ion batteries. Electrochim. Acta, 2007, 53: 1386-1393. https://doi.org/10.1016/j.electacta.2007.10.009.

[70] R. Jung, R. Morasch, P. Karayaylali, K. Phillips, F. Maglia, C. Stinner, Y. Shao-Horn, H.A. Gasteiger, Effect of ambient storage on the degradation of Ni-rich positive electrode materials (NMC811) for Li-ion batteries, J. Electrochem. Soc. 165 (2018) A132–A141, https://doi.org/10.1149/2.0401802jes.

[71] C.M. Julien, Lithium intercalated compounds charge transfer and related properties, Mater. Sci. Eng. R. Rep. 40 (2002) 47–102.

[72] B.V. Crist, Handbook of monochromatic XPS spectra: the elements of native oxides, John Wiley & Sons, 2000.

[73] M.C. Biesinger, B.P. Payne, A.P. Grosvenor, L.W.M. Lau, A.R. Gerson, R.S.C. Smart, Resolving surface chemical states in XPS analysis of first row transition metals, oxides and hydroxides: Cr, Mn, Fe, co and Ni, Appl. Surf. Sci. 257 (2011) 2717–2730.

[74] L. Baggetto, D. Mohanty, R.A. Meisner, C.A. Bridges, C. Daniel, D.L. Wood III, N. J. Dudney, G.M. Veith, Degradation mechanisms of lithium-rich nickel manganese cobalt oxide cathode thin films, RSC Adv. 4 (2014) 23364–23371.

[75] C. Busà, M. Belekoukia, M.J. Loveridge, The effects of ambient storage conditions on the structural and electrochemical properties of NMC-811 cathodes for Li-ion batteries, Electrochim. Acta 366 (2021) 137358, https://doi.org/10.1016/j.electacta.2020.137358.

[76] F. Friedrich, B. Strehle, A.T.S. Freiberg, K. Kleiner, S.J. Day, C. Erk, M. Piana, H. A. Gasteiger, Capacity fading mechanisms of NCM-811 cathodes in lithium-ion batteries studied by X-ray diffraction and other diagnostics, J. Electrochem. Soc. 166 (2019) A3760–A3774.

[77] C.S. Johnson, J.-S. Kim, C. Lefief, N. Li, J.T. Vaughey, M.M. Thackeray, The significance of the Li2MnO3 component in 'composite' xLi2MnO3·(1−x) LiMn0.5Ni0.5O2 electrodes, Electrochem. Commun. 6 (2004) 1085–1091, https://doi.org/10.1016/j.elecom.2004.08.002.

[78] C.P. Woodley, R.A. Cooper, B.M. Bartlett, Cu doping increases capacity retention in LiNi0. 6Mn0. 2Co0. 2O2 (NMC622) by altering the potential of the Ni-based redox couple and inhibiting particle pulverization, ACS Appl Energy Mater 7 (2024) 7875–7884.

[79] Hublikar, L. V, Ganachari, S. V, Shilar, F., Raghavendra, N. Recent advances in transition metal oxide nanomaterials for solar cell applications: a status review and technology perspectives. Mater. Res. Bull. (2025) 113351.

[80] I. McClelland, S.G. Booth, N.N. Anthonisamy, L.A. Middlemiss, G.E. Pérez, E. J. Cussen, P.J. Baker, S.A. Cussen, Direct observation of dynamic lithium diffusion behavior in nickel-rich, LiNi0. 8Mn0. 1Co0. 1O2 (NMC811) cathodes using operando muon spectroscopy, Chem. Mater. 35 (2023) 4149–4158.

[81] A.C. Lazanas, M.I. Prodromidis, Electrochemical impedance spectroscopy— a tutorial, ACS Measurement Science Au 3 (2023) 162–193.

[82] Talian, S.D., Brutti, S., Navarra, M.A., Moskon, J., Gaberscek, M. Impedance spectroscopy applied to lithium battery materials: good practices in measurements and analyses (69, 103413, 2024), Energy Storage Mater. 76 (2025).